






Accurate attenuation characterization in optical coherence tomography using multi-reference phantoms and deep learning

NIAN PENG,¹ CHENGLI XU,¹  YI SHEN,² WU YUAN,³  XIAOYU YANG,¹ CHANGHAI QI,⁴ HAIXIA QIU,⁵ YING GU,^{1,5} AND DEFU CHEN^{1,*} 

¹*School of Medical Technology, Beijing Institute of Technology, Beijing 100081, China*

²*Fujian Provincial Key Laboratory for Photonics Technology, Fujian Normal University, Fuzhou 350117, China*

³*Department of Biomedical Engineering, The Chinese University of Hong Kong, Hong Kong SAR 999077, China*

⁴*Department of Pathology, Aerospace Central Hospital, Beijing 100049, China*

⁵*Department of Laser Medicine, First Medical Center of PLA General Hospital, Beijing 100853, China*

*defu@bit.edu.cn

Abstract: The optical attenuation coefficient (AC), a crucial tissue parameter indicating the rate of light attenuation within a medium, enables quantitative analysis of tissue properties and facilitates tissue differentiation. Despite its growing clinical significance, accurate quantification of AC from optical coherence tomography (OCT) signals remains a pressing concern. This study comprehensively investigates the factors influencing the accuracy of quantitative AC extraction among existing OCT-based AC extraction algorithms. Subsequently, we propose an approach, the Multi-Reference Phantom Driven Network (MR-Net), which leverages multi-reference phantoms and deep learning to implicitly model factors affecting OCT signal propagation, thereby automatically regressing AC. Using a dataset from Intralipid and silicone-TiO₂ phantoms with known AC values obtained from a collimated transmission system and imaged with a 1300 nm swept-source OCT system, we conducted a thorough comparison focusing on data length, out-of-focus distance, and reference phantoms' attenuation among existing OCT-based AC extraction algorithms. By leveraging this extensive dataset, MR-Net can automatically model the complex physical effects in the transmission process of OCT signals, significantly enhancing the accuracy of AC predictions. MR-Net outperforms other algorithms in all metrics, achieving an average relative error of only 10.43% for calculating attenuation samples, significantly lower than the lowest value of 23.72% achieved by other algorithms. This method offers a quantitative framework for disease diagnosis, ultimately contributing to more accurate and effective tissue characterization in clinical settings.

© 2024 Optica Publishing Group under the terms of the [Optica Open Access Publishing Agreement](#)

1. Introduction

Optical coherence tomography (OCT) is an established technique that offers noninvasive, real-time, high resolution, three-dimensional visualization of tissue microstructure *in vivo* [1–5]. Moreover, the optical attenuation coefficient (AC) of tissue can be quantified by analyzing the depth-dependent decay of the OCT signal [6–9]. Recent studies have suggested that the onset and progression of diseases often correlate with tissue structural and functional changes, leading to alterations in tissue optical properties [10,11]. These changes in the AC reflect variations in tissue composition, such as water, lipids, and proteins. Optical attenuation is rapidly emerging as a crucial tool in disease diagnosis. The AC, measuring light fade speed through media, is becoming an effective diagnostic tool, helping distinguish diseased from healthy tissue.

Indeed, AC analysis has been used to quantify and distinguish various tissue types in preclinical and clinical studies across a wide range of medical fields. McLaughlin *et al.* was the first to experimentally demonstrate the application of parametric OCT attenuation imaging to assess cancer *ex vivo* by showing contrast between malignant and normal non-neoplastic tissue in malignant human axillary lymph nodes from breast cancer patients [12]. Studies such as that conducted by Carmen *et al.* in 2015 have shown that high- and low-grade brain cancer tissues had significantly lower optical attenuation values at both cancer sore and infiltrated zones when compared with noncancer matter, and they give a attenuation threshold of 5.5 mm^{-1} based on OCT detection [13]. Muller *et al.* used AC analysis to differentiate among benign stromal tissue, inflammation, and different grades of prostate cancer. The study demonstrates that there are significant median AC values among stroma, inflammation, Gleason 3, and Gleason 4 (4.6, 4.1, 5.9 and 5.0 mm^{-1}) [14]. Furthermore, determining the AC from OCT data also aids other *in vivo* diagnostics, such as differentiating healthy from cancerous bladder and colon tissue, visualizing atherosclerotic plaques, evaluating glaucoma, and imaging the cerebral cortex post-stroke, assessing vascularity in acne scars and burn, monitoring photodynamic therapy effects on skin lesions [10,11,15].

Various algorithms have been proposed to estimate the AC based on OCT data. The AC value was extracted from OCT imaging by two general models: the single-scattering (SS) model, which is suitable for the thin layer or low attenuation tissues, and the multiple-scattering (MS) model, which applies to high attenuation samples [10,15]. Typically, the SS model is more commonly used due to its simplicity, and numerous AC extraction algorithms are dedicated to this model. These SS model-based algorithms include methods such as exponential fitting (EF), logarithmic fitting (LF), and fast frequency domain algorithm (FD) for AC on a per A-line basis [16–19]. Additionally, depth-resolved (DR) and optimized depth-resolved estimation algorithm (ODRE) are used for extracting AC on a per-pixel basis [17–19].

As mentioned earlier, the use of OCT attenuation for tissue characterization is expanding, demonstrating promising contrast between healthy and diseased tissues. However, studies reveal significant variations in attenuation values for the same tissue types [10,15]. These substantial variations may be attributed to several factors, including unclear instrument configuration, different data processing methods, varying depth ranges for attenuation calculation, as well as issues with accuracy and precision. Firstly, a thorough comparison of detection sensitivity, range and estimation accuracy among OCT-based AC extraction algorithms is lacking. There are limited studies that have conducted systematic research on the accuracy of AC obtained from the target sample [20]. Secondly, all algorithms require calibration with OCT system-specific parameters for practical use. A notable challenge in AC estimation lies in compensating for the system-dependent effects that can affect algorithm accuracy. Factors like data length (in the z-direction) for analysis, the distance between sample surface and the OCT focal point, and the choice of reference phantom all affect accuracy. Modeling these effects is difficult, and quantitative studies remain unexplored. It's well known that the probability of few-scattering events increases with penetration depth, while the SS-based algorithm is primarily suited for areas with low scattering. Increasing the OCT data length for analysis increases the probability of few-scattering, thereby affecting accuracy. Additionally, variations in the distance between the sample surface and the OCT focus also affect the calculation accuracy, due to shifts in high signal-to-noise ratio (SNR) data regions and the influence of the confocal effect on precision. A prevalent approach to offset the system-dependent effects involves using computational methods along with a reference phantom with a known AC to normalize OCT signal from the sample. Given that the AC derives from signal intensity, the choice of reference phantom can impact the intensity of the normalized signal, consequently affecting the algorithm's accuracy.

In this study, we aimed to conduct a comprehensive study on the influencing factors for quantitative AC extraction. Furthermore, we developed a novel approach that integrates multi-reference phantoms and deep learning to accurately estimate AC. We performed a thorough comparison, focusing on influencing factors of data length, out-of-focus distance and the attenuation of reference phantoms evaluation for quantitative AC extraction among existing OCT-based AC extraction algorithms. These comparisons utilized phantoms with known AC values obtained from the collimated transmission system. Additionally, we proposed a high-precision AC calculation algorithm, Multi-Reference Phantom Driven Network (MR-Net), which leverages deep learning to implicitly model factors affecting OCT signal propagation, thereby automatically regressing AC of biological tissues. This work provides a high-precision AC calculation algorithm based on deep learning, which holds promise for advancing the clinical application of OCT in disease diagnosis and the delineation of tumor margins.

2. Methods

2.1. Attenuation coefficient estimation model

In the SS model, it is assumed that during the forward propagation of the incident beam, light scatters from the sample only once [16,21]. This process is modeled as an exponential decay, indicating that the detected signal power is directly proportional to the reflected intensity from sample, resulting from scattering at a specific depth. The depth-dependent average OCT signal can be expressed as follows:

$$A(z) = A_0 \sqrt{\frac{\mu_{bs}}{4\pi}} \cdot e^{-\mu_t \cdot (z-z_0)} \cdot h(z) \cdot U(z-z_0), \text{ where } U(z-z_0) = \begin{cases} 1 & \text{if } z \geq z_0 \\ 0 & \text{if } z < z_0 \end{cases} \quad (1)$$

where $A(z)$ is the OCT signal amplitude, z is the imaging depth, z_0 is the surface of the sample, A_0 is the overall system constant, μ_{bs} is the backscattering coefficient, μ_t is the total AC, and the $h(z)$ represent the point spread function of OCT system.

The EF method directly applies the exponential model of light transmission for parameter fitting. EF is highly resistant to the few-scattering effect, making it a benchmark for evaluating ACs in numerous studies [7,22]. The LF method convert Eq. (1) to a logarithmic model for fitting the AC.

The FD algorithm represents a novel approach that facilitates robust and efficient optical attenuation characterization. Standardized using a reference phantom, this method involves Fourier transforms and algebraic operations on the Eq. (1) [22]. The amplitude of harmonic coefficients is determined using the discrete Fourier transform:

$$|F_m(k = m \cdot \omega)| = \left| \sum_{n=0}^{N-1} A(n \cdot \Delta z) \cdot e^{-i \cdot k \cdot n \cdot \Delta z} \right| \quad (2)$$

where $\omega = \frac{2\pi}{N \cdot \Delta z}$ is the fundamental spatial frequency, Δz is the pixel size along the depth, and N is the total number of data points per A-line. The AC is obtained by comparing the amplitudes of any two harmonic coefficients in the Fourier domain, such as the ratio of the DC component to the modulus of the first harmonic system:

$$\beta = \frac{|F_0(k=0)|}{\left| F_1\left(k = \frac{2\pi}{N \cdot \Delta z}\right) \right|} = \frac{\sqrt{\left(\frac{2\pi}{N \cdot \Delta z}\right)^2 + (\mu_{ext}^s - \mu_{ext}^r)^2}}{(\mu_{ext}^s - \mu_{ext}^r)} \quad (3)$$

where N represents the total number of pixel data. Applying a discrete Fourier transform to Eq. (2) yields:

$$\alpha = \frac{|F_0(k=0)|}{|F_1(k=\frac{2\pi}{N\Delta z})|} = \frac{|\sum_{n=0}^{N-1} A(n\Delta z) \cdot e^{-i\cdot 0\cdot n\Delta z}|}{|\sum_{n=0}^{N-1} A(n\Delta z) \cdot e^{-i\cdot \frac{2\pi}{N\Delta z} \cdot n\Delta z}|} \quad (4)$$

The equation characterizes the relative attenuation between the test sample and the reference phantom. Given the AC of the reference phantom, substituting the total number of pixels, pixel size, and yield the AC of the sample.

Since the aforementioned methods operated over a specific depth range, they require sample uniformity. Thus, an A-line can only predict one AC. The depth-resolved method, proposed by Vermeer, determines the AC pixel-by-pixel by analyzing the OCT signal strength differences [17]. The DR method relies on two key assumptions: 1. All the light is attenuated along the OCT image depth range; 2. The fraction of backscattered light remains constant. Assuming constant intensity over a pixel, attenuation is expressed as:

$$\mu[i] \approx \frac{I[i]}{2\Delta \sum_{i+1}^N I[i]} \quad (5)$$

Here, N represents the number of pixels within a limited depth. However, in both simulation and practical applications, a bias in overestimating the AC at the end of the A-line will occur. To minimize this error, Liu *et al* developed the ODRE algorithm [18]. They determined the AC of the signal tail through curve fitting and integrated it into the formula to offset the trailing error. The AC for the last point N in DR can be expressed as:

$$\mu_t[N] = \frac{I[N]}{2\Delta \sum_{i=N+1}^{\infty} I[i]} \quad (6)$$

By combining formula (5) and (6), the AC at depth z is given by:

$$\mu_t[z] = \frac{I[z]}{2\Delta \sum_{i=z+1}^N I[i] + \frac{I[N]}{\mu_t[N]}} \quad (7)$$

2.2. Swept-source OCT system

As shown in Fig. 1(A), a swept-source OCT system with an axial resolution of $\sim 15 \mu\text{m}$ and a lateral resolution of $\sim 12 \mu\text{m}$, centered at 1300 nm , was used. The incident power on the samples was around 22 mW . At the baseline visit, scans of $5 \times 5 \text{ mm}^2$ were conducted, with 2048 pixels for each A-line and 500 A-lines per B-scan. Each B-scan was repeated four times and then averaged to perform initial denoising.

2.3. Phantom fabrication and ex vivo imaging procedure

To experimentally validate the accuracy of the proposed algorithm, we fabricated a series of liquid and solid phantoms with varying optical attenuation, following the established protocols [23]. These phantoms mimic a wide range of tissue optical properties, enabling comprehensive testing. Specifically, we created 20 liquid phantoms using Intralipid, with concentrations ranging from 0.125% to 20%, and crafted 12 solid phantoms incorporating TiO_2 , as shown in Fig. 1(B). The production of the liquid phantom is straightforward: the Intralipid was directly added to the base deionized water to achieve the desired concentration. The preparation process of the solid phantoms involved mixing TiO_2 power with the curing agent part of Sylgard 184 (Dow Corning). The mixture was then combined with the elastomer part of Sylgard 184 and blended for 30 minutes, maintaining a 10:1 ratio of curing agent to elastomer. To ensure homogeneity, the mixture was agitated for another 30 minutes using a blender, followed by ultrasonic treatment

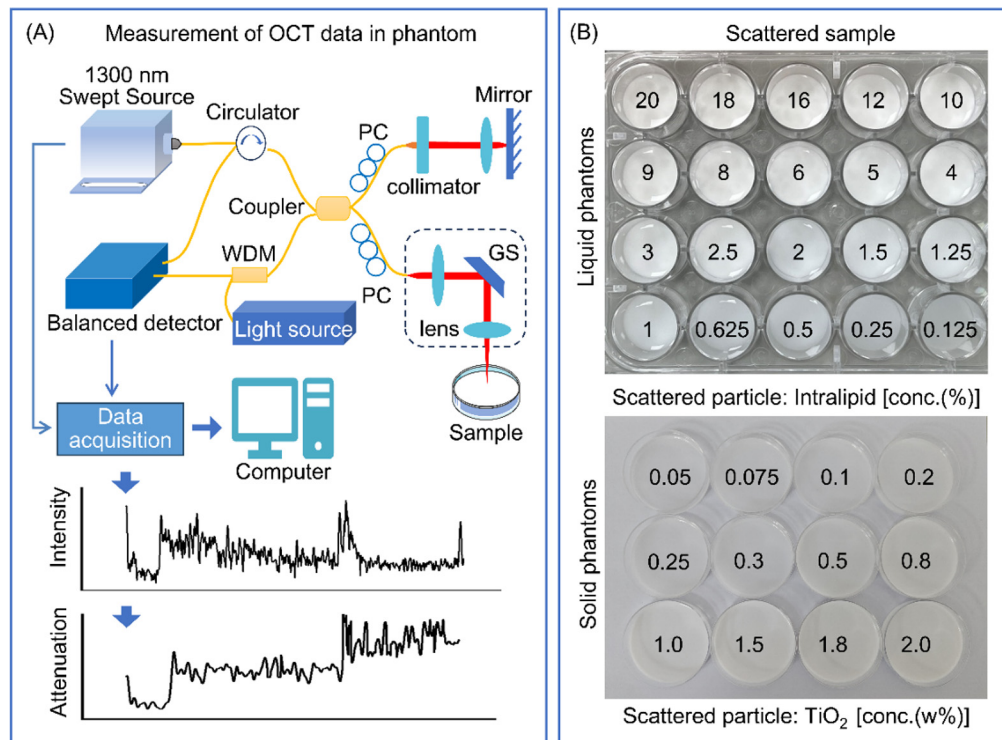


Fig. 1. Diagram of SS-OCT system and fabrication of the phantoms. (A) Schematic diagram of 1300 nm SS-OCT system, PC: Polarization controller; GS: Galvo scanning system; WDM: Wavelength division multiplexer. (B) The scattered samples used for measurement include both liquid and solid phantoms.

for 30 minutes to disperse any clusters. Subsequently, a vacuum pump was used to degas the mixture for 5 minutes, eliminating air bubbles. Through this process, 12 homogeneous phantoms with TiO₂ concentrations ranging from 0.05 to 2 weight percent were made separately.

Fresh mouse brain tissues were collected from euthanized Balb/c mice (8-11 weeks, SPF (Beijing) Biotechnology Co., Ltd., China). Post-harvest, brain tissue specimens were immediately cut with a knife and imaged with the swept-source OCT. The imaging protocol for the study was approved by Institutional Review Board and Research Ethics Committee of Beijing Institute of Technology.

2.4. Attenuation coefficient quantification of the phantoms

To establish a high quantitative research benchmark for the experiments presented in this paper, we use a collimated transmission system to quantify the AC of each phantom. Collimated transmission system is a widely recognized method for quantifying optical properties [24]. This approach determines the AC of samples by measuring their collimated transmission rates and applying Lambert-Beer's law. The procedure involves initially measuring the reference light intensity without the sample (known as a blank measurement), and then measuring the collimated transmission light intensity passing through the sample. After obtaining the collimated transmission rate, we integrated Lambert-Beer's law with this rate to derive the AC of the sample.

2.5. Experimental implementation and reference phantoms driven network (MR-Net)

The process of this study is shown in Fig. 2. As shown in Fig. 2(A), the study was carried out after calibration of target phantoms and acquisition of OCT data. First, for the purpose of analysis the factors that affect the quantitative AC algorithm, data length, AC of the reference phantoms and the sample location have been highlighted to explore its impact as shown in Fig. 2(B). To comprehensively assess their impact, we employed the five methods already mentioned above, LF, EF, FD, DR and ODRE. The application range of these algorithms is given under the optimum parameters. In response to the intricate interplay of these factors, as shown in Fig. 2(C), we propose a novel approach termed Multi-Reference Phantom Driven Network (MR-Net) for AC estimation. To gauge its efficacy, we compared the accuracy of this method against traditional methods. Quantitative evaluation of the method's accuracy was conducted by comparing the estimated AC with ground truth values obtained from the collimated transmission system [25]. Subsequently, we conducted application-oriented research on AC imaging utilizing these algorithms across both phantoms and mouse brains. The specific experiment is further discussed in following description.

The MR-Net method relies on the phantoms having known AC determined by the collimated transmission system. Considering that the AC of most human tissues falls within the 0 to 10 mm⁻¹ range, we used 20 liquid phantoms for training and testing. To ensure diversity in the training data and prevent overfitting, we collected four C-scans for each phantom at four distinct positions, with each C-scan containing 10 B-scans. Additionally, data were collected four times at each position and averaged for initial denoising.

The architecture of MR-Net is shown in the Fig. 2(C). The model for computing ACs comprises three primary components: the attenuation feature extraction module, the attenuation spatial reconstruction model, and the AC regression module. The attenuation feature extraction module employs an encoding structure consisting of several downsampling convolutional blocks. As the input signal scale decreases and the number of channels increases, a significant amount of redundant information is compressed. Low-dimensional spatial information gradually transforms into high-dimensional attenuation semantic features. The attenuation spatial reconstruction module adopts a decoding structure composed of several upsampling deconvolutional blocks. During the upsampling process, the same-scale feature maps from the attenuation feature extraction module are fused with the current-layer feature maps to regularize the attenuation spatial reconstruction process. This fusion serves as a regularization constraint, preventing the network divergence during training, thereby improving convergence speed and enhancing the stability of attenuation spatial reconstruction. The AC regression module is a fully connected network that outputs a scalar. This module takes the attenuation space features as input, combines and represents these features, and ultimately regresses them to AC.

During the dataset partitioning into training and testing sets, phantoms were initially categorized into four groups based on their AC: very low attenuation ($\leq 1 \text{ mm}^{-1}$), low attenuation ($1 \text{ mm}^{-1} \leq \text{AC} \leq 3.5 \text{ mm}^{-1}$), medium attenuation ($3.5 \text{ mm}^{-1} \leq \text{AC} \leq 5.5 \text{ mm}^{-1}$), and high attenuation ($\geq 5.5 \text{ mm}^{-1}$). This ensured that both the training and testing sets included data from phantoms representing various attenuation levels, while preventing data crossover by ensuring that all OCT data from the same phantom appeared exclusively in either the training or testing set. After comprehensive threshold calculation, feature vectors were truncated based on a threshold, excluding the invalid data at the beginning and end of each A-line. Consequently, the input vector for the network consisted of a one-dimensional vector with 1500 features.

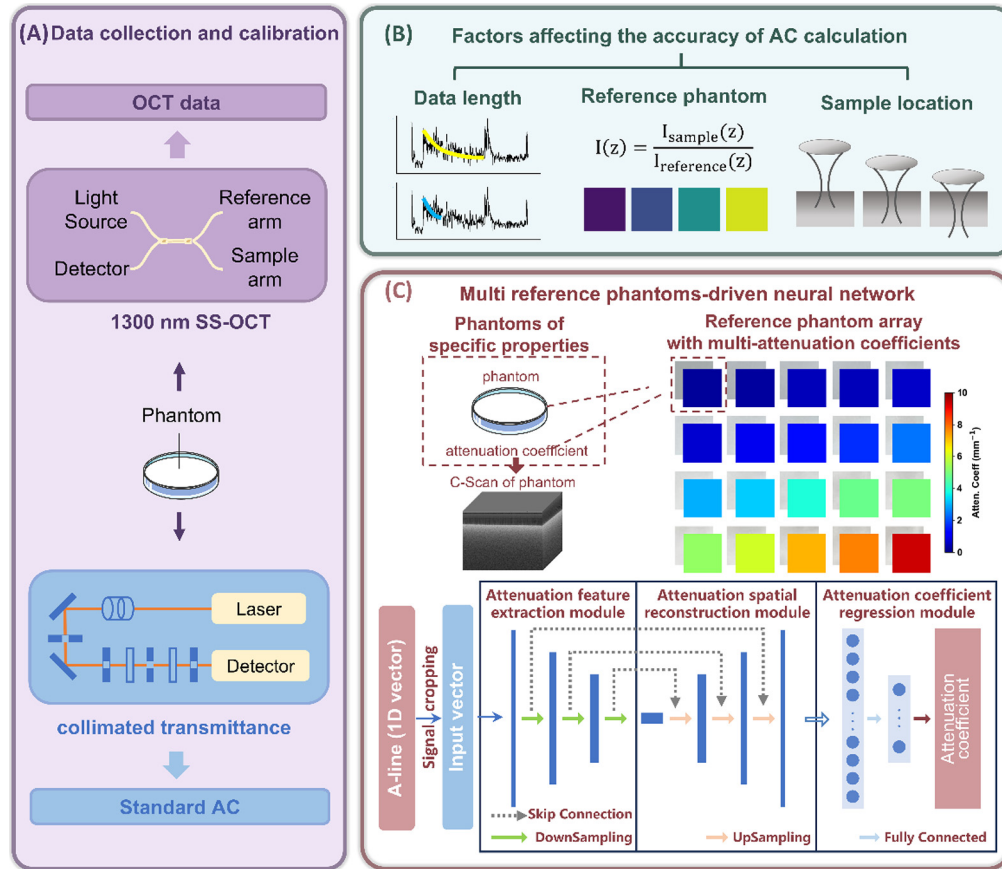


Fig. 2. Overview of the entire study process. (A) The OCT and the collimated transmission system were used to quantify the AC of each phantom. (B) Exploration of the influencing factors affecting AC results, including data length, reference phantom, and sample location, with particular emphasis on the distance from samples to the focal point. (C) Illustration of the MR-Net architecture for AC estimation, consisting of three primary components: the attenuation feature extraction module, the attenuation spatial reconstruction model, and the AC regression module. The training and testing sets included data from phantoms representing various attenuation levels.

3. Results

3.1. Investigation of the factors affecting quantitative extraction of AC

3.1.1. Comparison of accuracy and robustness against the data length

The first step involves evaluating the impact of data length (in the z-direction) on calculating the AC. While the EF, LF, FD, DR and ODRE methods are based on single scattering method, the few-scattering occurs in real-life conditions. In turbid media, increased data length raises scattering possibilities. Longer data length correspond to extended optical paths and more scattering, affecting precision, while shorter data provides less information for fitting, potentially leading to inaccurate results. Data lengths of 200, 250, 300, 350, 400, and 450 μm , which were most commonly used, were selected for comparison. The theoretical diagram is shown in Fig. 3(A). To evaluate the influence of data length on the AC across varying attenuation levels, we used liquid phantoms with Intralipid concentrations of 1%, 5%, 10%, and 16%, representing very low, low, medium, and high attenuation, respectively. By using the collimated transmission system, the true AC of these phantoms were determined as 0.56, 3.25, 5.29 and 7.16 mm^{-1} , respectively.

Since the DR algorithm assumes complete light attenuation within the imaging range, longer data lengths imply greater attenuation. Additionally, the ODRE algorithm's computation relies on EF and DR results. Therefore, this section focuses on discussing the impact of data length on the accuracy of A-line resolution algorithms. Figure 3(B) compared the AC obtained through EF, LF, and FD methods with the actual values. For medium and low attenuation regions, significant deviations were observed for short data lengths. However, when the data length exceeds 350 μm , the estimated results tend to stabilize, and all the methods yield values closer to the true one. Notably, accurate AC estimations remain elusive for high attenuation regions.

3.1.2. Comparison of accuracy and robustness against the distance between sample and focus of system

The relative position of the system focus to the sample significantly affects the quality of OCT imaging, with optimal imaging quality achieved at the system focus. If the sample lies below the focal plane, the high signal-to-noise ratio imaging near the zero optical path length may not be fully utilized, potentially compromising the accuracy of AC calculations. Conversely, when the OCT focus lies within the sample, a confocal effect may arise due to the focusing of Gaussian beams for transverse resolution, thereby affecting the algorithm's precision [26]. OCT data were collected across a range of distances between the sample surface and the system focus, ranging from -0.5 to 1.25 mm, with 11 data points. The ACs for the phantoms were 0.56, 3.25, 5.29 and 7.16 mm^{-1} . During data acquisition, the probe of the OCT probe was fixed while the sample was placed on an adjustable translation platform.

Figures 3(C) and 3(D) compared the calculated AC at various distances with the true values. As the distance shifts from negative to positive, the estimated values initially slightly increase then fall. When the distance is zero, indicating that the focal point is located on the sample surface, the calculated AC exhibits the highest agreement with the standard value. The estimation error increases with the distance between the focus and the sample surface.

3.1.3. Comparison of accuracy and robustness against the reference phantoms' AC

To determine AC, a reference phantom compensation system is often used to mitigate system-related effects. This process involves conducting measurements on a reference phantom and comparing them to the OCT signals obtained from the actual sample. However, inherent differences exist between the reference phantom and the sample, particularly in terms of optical attenuation path and scattering particle density. As the optical attenuation and scattering particle count in the reference phantom increases, the optical transmission effects become more complex.

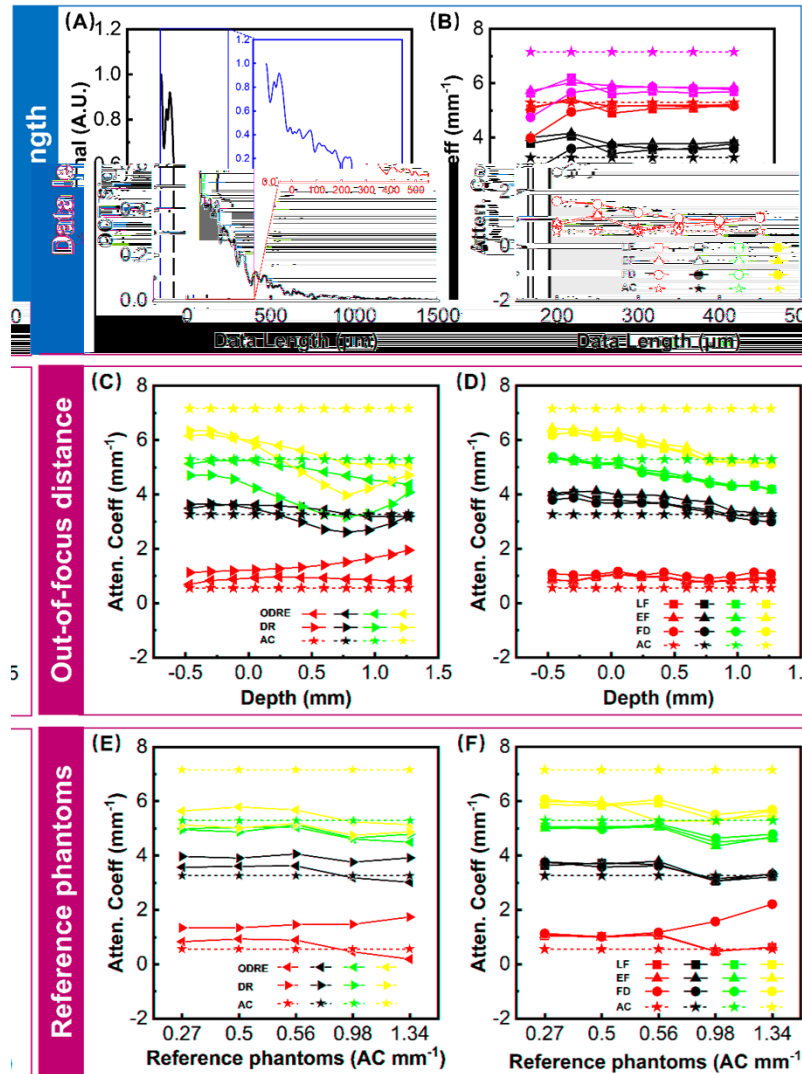


Fig. 3. Factors affecting quantitative extraction of the AC. (A) A line of raw data representing OCT signal for different data lengths. (B) The AC predicted by exponential fitting (EF), logarithmic fitting (LF), Fourier domain (FD) are compared with the ground truth under different data lengths, including 200, 250, 300, 350, 400, 450 μm . High (pink line), medium (red line), low (black line), and very low (blue line) AC values were calculated using LF (rectangles), EF (positive triangle), FD (circles) and compared with ground truth (AC, stars). (C) Comparison of accuracy and robustness against the distance between the sample surface and the focus of the system based on the pixel-resolved algorithm of optimized depth-resolved estimation algorithm (ODRE, left triangle) and depth-resolved (DR, right triangle). (D) Comparison of accuracy and robustness against the distance between the sample surface and the focus of the system based on the A-line-resolved algorithm of EF, LF and FD. (E) The extraction of AC by DR and ODRE using different reference phantoms. (F) The extraction of AC by EF, LF and FD using different reference phantoms.

We selected five light concentration phantoms as references, with ACs of 0.27, 0.5, 0.56, 0.98, 1.34 mm^{-1} , to evaluate which reference phantom most closely aligns with the ground truth. This helps compensate for system-related errors in AC calculations. For comparison, we also used the phantoms with the true AC of 0.56, 3.25, 5.29 and 7.16 mm^{-1} , representing different attenuation levels.

Figures 3(E) and 3(F) clearly indicate that as the AC increases, the calculations from various algorithms are greatly deviated from the standard value especially low-attenuation samples and some results are even negative, which greatly affects the calculation accuracy. In addition, the result represents that the calculation results are best when the AC of the reference form is less than 0.5 mm^{-1} . As in the previous section, highly attenuated phantoms cannot be accurately estimated whatever the attenuation degree of the reference phantom.

Based on the above research, the ACs were extracted in 20 liquid phantoms and 12 solid phantoms using EF, LF, FD, DR and ODRE algorithms, under the conditions of a data length of $350 \mu\text{m}$, with the sample surface located at the system's focal point, and a reference phantom with AC of 0.50 mm^{-1} for sample normalization. Subsequently, these extracted ACs were compared to the true values determined by the collimated transmission system. As shown in Fig. 4, the calculated values from various algorithms are close to the standard values, when the AC of the sample is less than or equal to 5.5 mm^{-1} , for both liquid and solid phantoms. However, when the AC exceeds 5.5 mm^{-1} , the calculated values from these algorithms are significantly lower than the true values. Regarding trends, as the phantom concentration increases, both the AC values derived from the algorithms and the standard values obtained from the collimated transmission system show an upward trend.

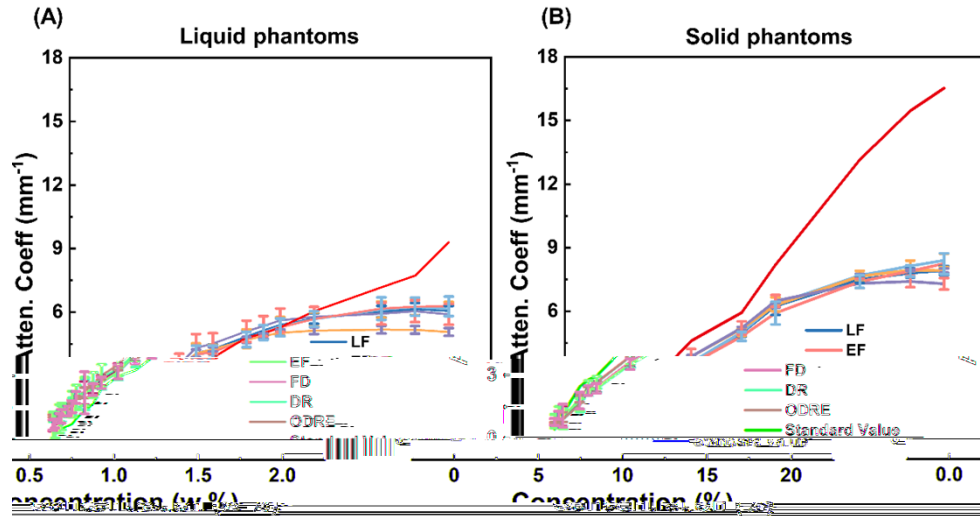


Fig. 4. Calculated values of the AC for 20 liquid and 12 solid phantoms, obtained using various methods: logarithmic fitting (LF, dark blue line), exponential fitting (EF, pink line), Fourier domain (FD, light blue line), depth-resolved (DR, orange line) and optimized depth-resolved (ODRE, purple line). These values are compared with the ground truth (red line). (A) Results for the liquid phantoms. (B) Results for the solid phantoms.

3.2. Proposed MR-Net based on deep learning for attenuation estimation

As previously mentioned, previous algorithms for calculating AC had limitations influenced by various factors, often requiring numerous parameters and underestimating high attenuation samples. To enhance accuracy and simplify the process, we introduced the MR-Net OCT

algorithm. This approach utilizes a deep learning dataset with multiple phantoms having known AC. MR-Net models the complex physical effects of OCT signal propagation, automatically compensating for system effects, and achieves precise AC estimation.

The mean square error between the network output of the estimation attenuation and the ground truth AC value is used as the loss function. The SGD (stochastic gradient descent) optimizer with a learning rate of 0.001 was used. And there were 200 epochs were considered with a batch of 32 was employed. After the model is trained, its performance is evaluated on the test set, which comprises five phantoms with AC ranging from 0.56 to 7.16 mm⁻¹. To evaluate the performance of the model on the test set, we employed metrics including mean relative error (MRE), mean absolute error (MAE), and root mean square error (RMSE). As shown in Table 1, the MRE of the model in estimating the AC of each phantom is less than 15%. The model can still provide relatively accurate calculation results for high attenuation samples that are underestimated by traditional SS models, thus compensating for the deficiencies of other methods. Overall, MR-Net demonstrates high calculation accuracy, indicating the feasibility of this method for estimating AC of samples with varying degrees of attenuation.

Table 1. The performance of MR-Net in test set

True AC (mm ⁻¹)	MRE (%)	MAE (mm ⁻¹)	RMSE (mm ⁻¹)
0.56	10.86	0.07	0.07
1.70	13.88	0.25	0.32
3.85	10.92	0.38	0.43
5.29	10.57	0.57	0.67
7.16	8.36	0.60	0.86

The results presented in Table 2 show that the proposed MR-Net algorithm outperforms traditional methods in all evaluated metrics, demonstrating its effectiveness in estimating AC for samples with medium and low attenuation, within the range of sample AC less than or equal to 5.5 mm⁻¹. Additionally, the computational accuracy of the other algorithms aligns with theoretical expectations and literature reports. Among these algorithms, EF performs best across all metrics, followed by FD and LF, which also rely on multi-feature data to provide AC results, thereby exhibiting high accuracy. Within pixel-by-pixel AC calculation algorithms, DR performs relatively poorly, while ODRE improves upon DR by optimizing and completing the attenuation at the tail of a single A-line, ultimately enhancing its accuracy.

Table 2. The performance of algorithms in low and medium attenuated phantoms

Algorithms	MRE (%)	MAE (mm ⁻¹)	RMSE (mm ⁻¹)
MR-Net	10.36	0.32	0.42
EF	23.42	0.39	0.49
LF	24.62	0.42	0.56
FD	31.27	0.47	0.60
DR	51.22	0.67	0.74
ODRE	46.71	0.71	0.94

Table 3 further shows a comprehensive performance comparison among six algorithms across all levels of attenuation included in this study. MR-Net consistently maintains its superior computational performance within this sample range. The results indicate that MR-Net outperforms the other algorithms in all metrics, achieving an MRE of only 10.43%, which is significantly lower than the lowest value of 23.72% attained by any of the other algorithms. Its performance is comparable to that in the medium and low attenuation sample range, proving

its stability across varying attenuation levels. However, the MAE and RMSE metrics for other algorithms worsen, indicating a decline in their computational accuracy for samples across all levels of attenuation, as compared to those with medium and low attenuation levels. A box plot illustrating the relative errors of all algorithms across all attenuation levels included in this study is presented in Fig. 5. It's evident from the figure that the MR-Net algorithm exhibits the smallest relative error, and its overall error distribution is the narrowest. The findings demonstrate that the proposed MR-Net method outperforms traditional approaches in all evaluated metrics, thereby validating the efficacy of the MR-Net method in estimating AC across all levels of attenuation.

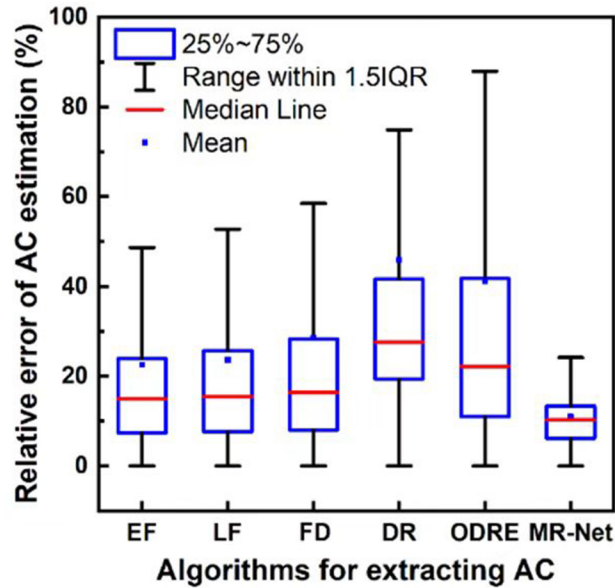


Fig. 5. Comparison of relative error in AC estimation across all levels of attenuation among six algorithms: EF, LF, FD, DR, ODRE, and MR-Net.

Table 3. The performance of algorithms across all levels of attenuation included in this study

Algorithms	MRE (%)	MAE (mm ⁻¹)	RMSE (mm ⁻¹)
MR-Net	10.43	0.35	0.56
EF	23.72	0.59	0.89
LF	24.68	0.63	0.93
FD	29.07	0.64	0.91
DR	46.61	0.91	1.02
ODRE	41.21	0.86	1.04

3.3. Validation of the MR-Net method for phantoms and tissues

As shown in Fig. 6(A), imaging of AC was performed on four liquid phantoms with significant attenuation differences using MR-Net and other five algorithms, and the results were compared

with the true values provided by the collimated transmission system. Figure 6(A) reveals that when sample attenuation is below 6 mm^{-1} , all tested algorithms align with the standard values in color mapping. However, the MR-Net algorithm exhibits a higher concordance with the standard values. For sample attenuation above 6 mm^{-1} , the other five algorithms display evident calculation deviations, with imaging results significantly divergent from the standard values. Conversely, the MR-Net algorithm remains robust, providing AC estimates close to the standard values. This underscores the broader applicable scope of the MR-Net algorithm in calculating AC and highlights its unique advantages in handling highly scattering samples, which are challenging to accurately estimate using traditional single-scattering models.

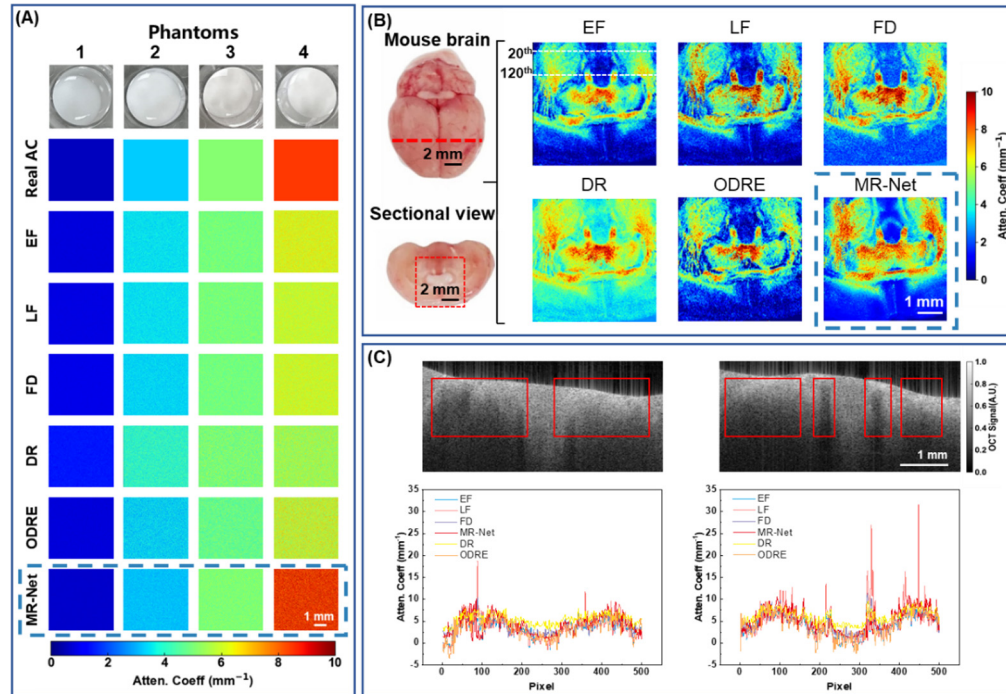


Fig. 6. Results of AC estimates from phantoms and mouse brain tissue. (A) AC map of liquid phantoms generated using six algorithms: EF, LF, FD, DR, ODRE, and MR-Net. (B) AC map of mouse brain sections. The AC of the region within the red box on the brain section were analyzed using the EF, LF, FD, MR-Net, DR and ODRE algorithms. (C) Quantitative comparison of the AC in the 20th and 120th frames of B-Scan OCT data for mouse brain sections.

To further validate the feasibility of MR-Net, we tested it on fresh mouse brain tissue using six algorithms: EF, LF, FD, DR, ODRE, and MR-Net. The resulting AC images of the mouse brain section are shown in Fig. 6(B), demonstrating that all six algorithms can provide clear mouse brain morphology and delineate the white-gray matter boundary. Notably, the AC of gray matter is significantly lower, while that of white matter is notably higher. Among the algorithms, MR-Net provides the most distinct contrast in the AC map. The contrast of the AC maps obtained using DR is less pronounced compared to those produced by the other algorithms. Subsequently, quantitative comparisons of the AC were conducted on the 20th and 120th B-Scans, which exhibit a continuous and significant change in the value of the AC. Physical images of the B-Scans and the attenuation curves for each algorithm in these frames are presented in Fig. 6(C). All algorithms provide relatively high estimates of the AC in regions of high attenuation (highlighted in red boxes). The attenuation curves generated by the MR-Net algorithm exhibit a relatively

smooth profile with minimal outliers, indicating the superior stability of the MR-Net algorithm compared to the other algorithms tested.

4. Discussions and conclusion

The application of OCT attenuation in tissue characterization is expanding, showing promising contrast between healthy and diseased tissue. However, studies have revealed significant variations in attenuation values for the same tissue types [10,15], highlighting the pressing concern of accurately quantifying AC derived from OCT. In this study, we quantitatively analyze the underlying causes and associated consequences of the underestimation and overestimation issues inherent in the existing method employing phantoms with AC quantified with a collimated transmission system. We conduct a comprehensive comparison focusing on factors such as data length, out-of-focus distance, and the evaluation of reference phantoms' attenuation among OCT-based AC extraction algorithms. Furthermore, we propose an approach based on multi-reference phantoms to determine the AC from OCT which is to let the network learn to model the intricacies and complexities of the physical effects encountered during OCT signal propagation, automatically compensates for system effects affecting OCT signal propagation, and achieves precise regression of AC.

Each algorithm for calculating AC in OCT has its unique strengths and limitations. The EF method is robust but time-consuming due to its iterative process, while the LF method is faster but sensitive to few-scattering events, particularly in heterogeneous or highly scattering tissues. Both EF and LF methods are affected by the tissue surface position and lose accuracy with non-flat or dynamic surfaces. Conversely, the FD method is robust against incorrect surface detection but struggles with noise in thin-layer tissues, which can affect algorithm stability and AC accuracy [22]. DR improves accuracy with pixel-wise AC extraction, and ODRE enhances this with fitting methods for tail-end A-line calculations, but both require uniform samples and are susceptible to noise [27].

Notably, the accuracy and precision of OCT attenuation measurements have not been thoroughly examined in most research, contributing to wide variations in estimated attenuation values. Previous studies on AC extraction lacked a quantitative standard to assist in comparing the AC extracted from target samples using various algorithms. In this study, we determined the influencing factors on AC estimation, as well as the detection range and the accuracy of the AC extraction algorithm, based on a batch of phantoms with known AC determined using a collimated transmission system. Therefore, this study serves as a reference for comparing the attenuation values of the same tissue types across different studies that use different extraction algorithms.

In the process of determining AC through fitting methods, the length of data included in the calculation plays a crucial role in ensuring accuracy. Most biological tissues exhibit average AC below 6 mm^{-1} [10], and a majority of algorithms can accurately estimate the AC within the range. When the data length is $350 \mu\text{m}$, the AC of the reference phantom is less than 0.5 mm^{-1} , and with the focal point of the system is positioned on the surface of the target sample, the estimated attenuation value is closest to the true value. However, when the data length is short, significant disparities arise in the attenuation values estimated by various algorithms, leading to substantial standard deviations in the results generated by individual methods. The discrepancy is attributed to the limited number of data points available for algorithmic computation, which induces pronounced variations in the calculated results [15]. When the data length is greater than or equal to $350 \mu\text{m}$, the calculation result becomes stable. Yet, as the data length continues to expand, the optical transmission model (i.e., SS model) employed for fitting the AC may lose its validity. Consequently, we did not explore the performance of higher data length in this study. Nevertheless, Yuan *et al.*'s study observed notable disparities in the calculated values of various algorithms when the data length reached $1000 \mu\text{m}$, particularly for high attenuation

scenarios, highlighting the importance of considering data length for accuracy [22]. Yuan *et al.* also evaluated the robustness of LF, EF, and FD algorithms within a data length range of 350 to 1050 μm , finding high robustness for the FD algorithm in this range. Our study, focusing on a smaller range (200 to 450 μm), investigated high-precision AC calculations. Our results show that the FD algorithm's robustness decreases when data length is below 350 μm , which does not contradict Yuan *et al.*'s findings due to minimal overlap in the considered data lengths.

Reference phantoms are frequently used to mitigate the system influences on the AC estimation, yet there is a lack of research examining their impact on target sample calculations. Our findings reveal that when the attenuation degree of the reference phantom is less than or equal to 1.34 mm^{-1} , the LF, EF, DR, and ODRE algorithms maintain their calculation accuracy. However, the FD algorithm is sensitive to the attenuation degree of the reference phantom. The FD algorithm obtains the AC of a sample by normalizing the sample and deriving its relative attenuation compared to the reference phantom. As the reference phantom's attenuation increases, calculated values for low-attenuation samples deviate from the true values, suggesting that for accurate FD calculations, the reference phantom's AC should be lower. The DR and ODRE algorithms show similar trends, but the ODRE algorithm's results are closer to true values, indicating its compensation for A-line tail light attenuation enhances the DR algorithm's accuracy. Our results demonstrate that lower AC in reference phantoms yield more accurate calculations across all algorithms. Notably, significant discrepancies, including negative values, arise in phantom AC calculations when the sample's AC matches the reference phantom's, which is crucial to consider in ultra-low AC phantom calculations. Thus, when eliminating AC calculations based on reference phantoms without incorporating multiple scattering, it is prudent to select a suitable reference phantom considering the sample AC and the algorithm's dependence on the reference phantom's attenuation.

When examining the relative position of the sample and the system's focal point, variations in positions impact the intensity of light entering the sample. As the sample moves further away from the system's focal point, the trend of change in the calculated results of the A-line resolution algorithm becomes more pronounced. This trend is even more evident when the focal point is outside the sample, possibly due to the lower signal-to-noise ratio of sample imaging at greater defocus distances, which introduces more noise into the calculations and affects the computed AC [28]. At the same defocus distance, there is a clear gradient trend in the calculated results for samples with different degrees of attenuation, indicating that the defocus distance from the sample surface does not affect the relative results calculated by the LF, EF, and FD algorithms for samples with different attenuation levels. Specifically, when the system's focal point resides within the sample, the confocal effect influences the overall calculation performance [29,30]. Numerous previous studies have diligently examined the repercussions associated with this influential factor and attempted to eliminate it, and our study also proves that the factor does affect the accuracy of AC calculation [31].

The precise calculation of ACs is critically dependent on the careful management of various influencing factors, including instrument and measurement configuration, as well as key data processing parameters and methods. To address this, we introduced MR-Net, a deep learning-based approach that utilizes the A-line data from multi-reference phantoms to estimate optical AC. MR-Net, as a data-driven algorithm, learns the mapping patterns between OCT detection optical signals and AC directly from large-scale reference phantom A-line data [32]. The training data consists solely of individual A-lines without averaging. By leveraging this extensive dataset, MR-Net can automatically model the complex physical effects in the transmission process of OCT signals, significantly enhancing the accuracy of AC predictions. The AC of tissues varies significantly, with different AC ranges dictating the selection of appropriate algorithms for calculation. Most tissues, including kidney tissue ($3\text{--}5 \text{ mm}^{-1}$) [33,34], gray matter ($2\text{--}5 \text{ mm}^{-1}$) [13,35], ovarian cancer ($1\text{--}3 \text{ mm}^{-1}$) [36,37], typically exhibit low AC, enable accurate computed

by most algorithms. Conversely, tissues such as arterial tissue ($5\text{--}10\text{ mm}^{-1}$) [7,38] and white matter ($6\text{--}7.5\text{ mm}^{-1}$) [13,39] possess higher ACs, posing challenges for traditional algorithms to determine the absolute AC value accurately. Notably, MR-Net excels in providing precise calculations for these tissues, ensuring their clinical feasibility.

The application of the U-Net architecture has gradually expanded to regression tasks [40,41]. In 2022, Birdi *et al.* proposed a one-dimensional ultrasonic attenuation signal estimation method based on an improved U-Net, addressing the issue of multiple influencing factors in traditional ultrasonic signal AC calculations [42]. Compared to traditional model estimation methods, this approach offered higher overall accuracy. These applications demonstrate the superior performance of U-Net in regression tasks. In this study, we design the MR-Net network based on U-Net for AC regression, where the input data are OCT signals and the output is the corresponding AC of the signals. In constructing the network model, we adopt a modular design strategy, subdividing the model into three modules: attenuation feature extraction module, attenuation spatial reconstruction module, and AC regression module. The attenuation feature extraction module is responsible for mapping attenuation signals that can represent the optical parameter information of the sample structure to a high-dimensional space. The attenuation spatial reconstruction module then transforms signals from the physical space into feature representations in the attenuation space. Finally, the AC regression module combines and represents these attenuation features to achieve precise regression of the AC. Based on this design, MR-Net not only improves the accuracy of AC calculation but also enhances the model's interpretability and generalization ability. The results indicate that MR-Net outperforms other algorithms in all metrics, with an average relative error of only 10.43% for calculating attenuation samples, significantly lower than the lowest value of 23.72% achieved by other algorithms. It should be noted that, to simplify the calculation, numerous studies directly use the single scattering model to calculate the AC, although this model is only suitable for thin-layer samples or low-scattering samples. MR-Net has demonstrated excellent performance in both simplified models and wide detection ranges, accurately calculating the AC of high attenuation samples. The comparative analysis reveals that our algorithm is capable of delivering relatively precise estimates of AC without the need for prior parameter input. This underscores the efficacy of applying deep learning to AC estimation. Nevertheless, a critical factor that can significantly affect the calculation precision of MR-Net is the calibration accuracy of the reference phantoms. If the measured AC of these phantoms deviate considerably from their true values, the model may incorrectly learn the mapping relationship between the OCT signal and the AC. This mislearned relationship, in turn, can ultimately undermine the overall accuracy of MR-Net.

MR-Net's high-precision in calculating ACs lays a solid foundation for clinical use. It excels at detecting minor differences in these coefficients, enabling it to distinguish between healthy and diseased tissues. This capability is particularly invaluable in diagnosing a wide range of cancers, including those affecting the brain, kidney, and liver. Ultimately, MR-Net's versatility and accuracy present tremendous opportunities for enhancing diagnostic precision in clinical environments.

This study has several limitations. Firstly, while focusing on the commonly used single-scattering model for OCT-based AC extraction algorithms research to simplify calculations, it acknowledges the potential of multi-scattering models and full electromagnetic wave modeling for more precise OCT signal modeling. Future research should consider these models to deepen the understanding of OCT signal propagation mechanisms and enhance the theoretical foundation for AC calculations. Secondly, regarding deep learning-based AC calculation, accuracy can be improved by expanding the dataset and exploring different network models and loss functions. The current dataset, based on 20 reference phantoms, may limit model accuracy due to the phantom attenuation range and gradient. Expanding the dataset with a wider attenuation range and refining the attenuation gradient can provide richer information for model training. Additionally,

exploring more network models and loss functions tailored to OCT signal characteristics can further improve calculation accuracy and efficiency. Furthermore, to ensure the comprehensive inclusion of sample information, our study has concentrated solely on the precise calculation of the AC for single uniform structures. However, the algorithm's accuracy in determining the ACs for multi-layer structures is still being investigated. Lastly, while this study conducted quantitative imaging analysis on phantoms and animals, the limited sample size is not sufficient to fully demonstrate the practical application value of MR-Net. Large-scale tissue AC imaging is needed to further verify the practical application of MR-net and explore the relationship between tissue pathology and AC changes.

In conclusion, we conducted a comprehensive study on the influencing factors of quantitative AC extraction and developed a new approach that combines multi-reference phantom and deep learning to accurately estimate AC. Our experimental results consistently demonstrated that the MR-Net outperforms traditional methods such as EF, LF, FD, DR, and ODRE, regardless of whether the target sample exhibits low or high attenuation. Our study shows the potential of using multi-reference phantoms for enhancing accuracy and universality, as well as the efficacy of deep learning for regressing biological parameters. Furthermore, this work provides a high-precision AC calculation algorithm based on deep learning, which promotes the clinical application of OCT in disease diagnosis and the delineation of tumor margins in the future.

Funding. Beijing Municipal Natural Science Foundation (7222309); National Natural Science Foundation of China (62205025, 62227823); Beijing Institute of Technology Research Fund Program for Young Scholars (XSQD-202123001).

Disclosures. The authors declare no conflicts of interest related to this article.

Data availability. Data underlying the results presented in this paper are not publicly available at this time but may be obtained from the authors upon reasonable request.

References

1. A. Swaan, B. G. Muller, L. S. Wilk, *et al.*, "One-to-one registration of en-face optical coherence tomography attenuation coefficients with histology of a prostatectomy specimen," *J. Biophotonics* **12**(4), e201800274 (2019).
2. K. Y. Foo, K. Newman, Q. Fang, *et al.*, "Multi-class classification of breast tissue using optical coherence tomography and attenuation imaging combined via deep learning," *Biomed. Opt. Express* **13**(6), 3380–3400 (2022).
3. N. Wang, C.-Y. Lee, H.-C. Park, *et al.*, "Deep learning-based optical coherence tomography image analysis of human brain cancer," *Biomed. Opt. Express* **14**(1), 81–88 (2023).
4. S. Yuan, C. Xu, B. Cui, *et al.*, "Motor-free telerobotic endomicroscopy for steerable and programmable imaging in complex curved and localized areas," *Nat. Commun.* **15**(1), 7680 (2024).
5. T. Zhang, S. Yuan, C. Xu, *et al.*, "PneumaOCT: pneumatic optical coherence tomography endoscopy for targeted distortion-free imaging in tortuous and narrow internal lumens," *Sci. Adv.* **10**(35), eadp3145 (2024).
6. W. Yuan, D. Chen, R. Sarabia-Estrada, *et al.*, "Theranostic OCT microneedle for fast ultrahigh-resolution deep-brain imaging and efficient laser ablation *in vivo*," *Sci. Adv.* **6**(15), eaz9664 (2020).
7. C. Xu, J. M. Schmitt, S. G. Carlier, *et al.*, "Characterization of atherosclerosis plaques by measuring both backscattering and attenuation coefficients in optical coherence tomography," *J. Biomed. Opt.* **13**(3), 034003 (2008).
8. D. Chen, W. Yuan, H.-C. Park, *et al.*, "In vivo assessment of vascular-targeted photodynamic therapy effects on tumor microvasculature using ultrahigh-resolution functional optical coherence tomography," *Biomed. Opt. Express* **11**(8), 4316–4325 (2020).
9. K. Li, Q. Wu, S. Feng, *et al.*, "In situ detection of human glioma based on tissue optical properties using diffuse reflectance spectroscopy," *J. Biophotonics* **16**(11), e202300195 (2023).
10. P. Gong, M. Almasian, G. van Soest, *et al.*, "Parametric imaging of attenuation by optical coherence tomography: review of models, methods, and clinical translation," *J. Biomed. Opt.* **25**(04), 1 (2020).
11. K. Barwari, D. M. de Bruin, D. J. Faber, *et al.*, "Differentiation between normal renal tissue and renal tumours using functional optical coherence tomography: a phase I *in vivo* human study," *BJU Int* **110**(8B), E415–E420 (2012).
12. R. A. McLaughlin, L. Scolaro, P. Robbins, *et al.*, "Parametric imaging of cancer with optical coherence tomography," *J. Biomed. Opt.* **15**(4), 046029 (2010).
13. C. Kut, K. L. Chaichana, J. F. Xi, *et al.*, "Detection of human brain cancer infiltration *ex vivo* and *in vivo* using quantitative optical coherence tomography," *Sci. Transl. Med.* **7**(292), 292ra100 (2015).
14. B. G. Muller, R. A. A. van Kollenburg, A. Swaan, *et al.*, "Needle-based optical coherence tomography for the detection of prostate cancer: a visual and quantitative analysis in 20 patients," *J. Biomed. Opt.* **23**(08), 086001 (2018).
15. S. Chang and A. K. Bowden, "Review of methods and applications of attenuation coefficient measurements with optical coherence tomography," *J. Biomed. Opt.* **24**(09), 090901 (2019).

16. L. Thrane, H. T. Yura, and P. E. Andersen, "Analysis of optical coherence tomography systems based on the extended Huygens-Fresnel principle," *J. Opt. Soc. Am. A* **17**(3), 484–490 (2000).
17. K. A. Vermeer, J. Mo, J. J. A. Weda, *et al.*, "Depth-resolved model-based reconstruction of attenuation coefficients in optical coherence tomography," *Biomed. Opt. Express* **5**(1), 322–337 (2014).
18. J. Liu, N. Ding, Y. Yu, *et al.*, "Optimized depth-resolved estimation to measure optical attenuation coefficients from optical coherence tomography and its application in cerebral damage determination," *J. Biomed. Opt.* **24**(03), 035002 (2019).
19. K. Li, W. Liang, Z. Yang, *et al.*, "Robust, accurate depth-resolved attenuation characterization in optical coherence tomography," *Biomed. Opt. Express* **11**(2), 672–687 (2020).
20. L. B. Neubrand, T. G. van Leeuwen, and D. J. Faber, "Precision of attenuation coefficient measurements by optical coherence tomography," *J. Biomed. Opt.* **27**(08), 085001 (2022).
21. T. G. van Leeuwen, D. J. Faber, and M. C. Aalders, "Measurement of the axial point spread function in scattering media using single-mode fiber-based optical coherence tomography," *IEEE J. Select. Topics Quantum Electron.* **9**(2), 227–233 (2003).
22. W. Yuan, C. Kut, W. Liang, *et al.*, "Robust and fast characterization of OCT-based optical attenuation using a novel frequency-domain algorithm for brain cancer detection," *Sci. Rep* **7**(1), 44909 (2017).
23. D. M. de Bruin, R. H. Bremmer, V. M. Kodach, *et al.*, "Optical phantoms of varying geometry based on thin building blocks with controlled optical properties," *J. Biomed. Opt.* **15**(2), 025001 (2010).
24. L. Waszczuk, J. Ogien, F. Pain, *et al.*, "Determination of scattering coefficient and scattering anisotropy factor of tissue-mimicking phantoms using line-field confocal optical coherence tomography (LC-OCT)," *J. Eur. Opt. Society-Rapid Publ.* **19**(2), 39 (2023).
25. D. Levitz, L. Thrane, M. H. Frosz, *et al.*, "Determination of optical scattering properties of highly-scattering media in optical coherence tomography images," *Opt. Express* **12**(2), 249–259 (2004).
26. S. Stefan, K.-S. Jeong, C. Polucha, *et al.*, "Determination of confocal profile and curved focal plane for OCT mapping of the attenuation coefficient," *Biomed. Opt. Express* **9**(10), 5084–5099 (2018).
27. S. Zheng, Y. Fei, and S. Jian, "Method for parametric imaging of attenuation by intravascular optical coherence tomography," *Biomed. Opt. Express* **12**(4), 1882–1904 (2021).
28. B. Ghafaryasl, K. A. Vermeer, J. Kalkman, *et al.*, "Analysis of attenuation coefficient estimation in Fourier-domain OCT of semi-infinite media," *Biomed. Opt. Express* **11**(11), 6093–6108 (2020).
29. N. Dwork, G. T. Smith, T. Leng, *et al.*, "Automatically determining the confocal parameters from OCT B-Scans for quantification of the attenuation coefficients," *IEEE Trans. Med. Imaging* **38**(1), 261–268 (2019).
30. J. Kubler, V. S. Zoutenbier, A. Amelink, *et al.*, "Investigation of methods to extract confocal function parameters for the depth resolved determination of attenuation coefficients using OCT in intralipid samples, titanium oxide phantoms, and *in vivo* human retinas," *Biomed. Opt. Express* **12**(11), 6814–6830 (2021).
31. L. D. Fiske, M. C. G. Aalders, M. Almasian, *et al.*, "Bayesian analysis of depth resolved OCT attenuation coefficients," *Sci. Rep* **11**(1), 2263 (2021).
32. Y. Zhang, L. Kang, I. H. M. Wong, *et al.*, "High-throughput, label-free and slide-free histological imaging by computational microscopy and unsupervised learning," *Adv. Sci.* **9**(2), e2102358 (2022).
33. K. Barwari, D. M. de Bruin, E. C. C. Cauberg, *et al.*, "Advanced diagnostics in renal mass using optical coherence tomography: a preliminary report," *J. Endourol* **25**(2), 311–315 (2011).
34. M. Buijs, P. G. K. Wagstaff, D. M. de Bruin, *et al.*, "An *in-vivo* prospective study of the diagnostic yield and accuracy of optical biopsy compared with conventional renal mass biopsy for the diagnosis of renal cell carcinoma: the interim analysis," *Eur. Urol. Focus* **4**(6), 978–985 (2018).
35. M. Almasian, L. S. Wilk, P. R. Bloemen, *et al.*, "Pilot feasibility study of *in vivo* intraoperative quantitative optical coherence tomography of human brain tissue during glioma resection," *J. Biophotonics* **12**(10), e201900037 (2019).
36. Y. Yang, T. H. Wang, N. C. Biswal, *et al.*, "Optical scattering coefficient estimated by optical coherence tomography correlates with collagen content in ovarian tissue," *J. Biomed. Opt.* **16**(9), 090504 (2011).
37. Y. Yang, T. Wang, X. Wang, *et al.*, "Quantitative analysis of estimated scattering coefficient and phase retardation for ovarian tissue characterization," *Biomed. Opt. Express* **3**(7), 1548–1556 (2012).
38. F. J. van der Meer, D. J. Faber, D. M. B. Sassoon, *et al.*, "Localized measurement of optical attenuation coefficients of atherosclerotic plaque constituents by quantitative optical coherence tomography," *IEEE Trans. Med. Imaging* **24**(10), 1369–1376 (2005).
39. K. S. Yashin, E. B. Kiseleva, A. A. Moiseev, *et al.*, "Quantitative nontumorous and tumorous human brain tissue assessment using microstructural co- and cross-polarized optical coherence tomography," *Sci. Rep* **9**(1), 2024 (2019).
40. O. Ronneberger, P. Fischer, and T. Brox, "U-net: convolutional networks for biomedical image segmentation," in *18th International Conference on Medical Image Computing and Computer-Assisted Intervention (MICCAI)*, Lecture Notes in Computer Science 2015), 234–241.
41. C. Zhou, S. Wang, Z. Wang, *et al.*, "Absorption attenuation compensation using an end-to-end deep neural network," *IEEE T. Geosci. Remote* **60**, 1–9 (2022).
42. J. Birdi, J. D'Hooge, A. Bertrand, *et al.*, "A neural network approach for ultrasound attenuation coefficient estimation," in *30th European Signal Processing Conference (EUSIPCO)*, European Signal Processing Conference (2022), 902–906.